1   REVISION 1

2   Word count: 6367

3   **Hydroxylpyromorphite, modern description and**

4   **characterization of a mineral important to lead-remediation**

5   Travis A. Olds[1*], Anthony R. Kampf[2], John F. Rakovan[3], Peter C. Burns[4,5],
6   Owen P. Mills[6], and Cullen Laughlin-Yurs[7]
7
8   [1] Section of Minerals and Earth Sciences, Carnegie Museum of Natural
9   History, 4400 Forbes Avenue, Pittsburgh, Pennsylvania 15213, USA
10   [2] Mineral Sciences Department, Natural History Museum of Los Angeles
11   County, 900 Exposition Boulevard, Los Angeles, CA 90007, USA
12   [3] Department of Geology and Environmental Earth Science, Miami
13   University, Oxford, OH 45056, USA
14   [4] Department of Civil and Environmental Engineering and Earth Sciences,
15   University of Notre Dame, Notre Dame, IN 46556, USA
16   [5] Department of Chemistry and Biochemistry, University of Notre Dame,
17   Notre Dame, IN 46556, USA
18   [6] Applied Chemical and Morphological Analysis Laboratory, Michigan
19   Technological University, Houghton, MI 49931, USA
20   [7] 513 Iron Street, Norway, MI 49870, USA
21
22   *E-mail: oldst@carnegiemnh.org

23   **Abstract**

24   Hydroxylpyromorphite, $Pb_5(PO_4)_3(OH)$, has been documented in the literature

25   as a synthetic and naturally occurring phase for some time now but has not

26   previously been formally described as a mineral. It is fully described here for

27   the first time using crystals collected underground in the Copps mine, Gogebic

28   County, Michigan. Hydroxylpyromorphite occurs as aggregates of randomly

29   oriented hexagonal prisms, primarily between about 20 – 35 µm in length and

30   6 – 10 µm in diameter. The mineral is colorless and translucent with vitreous

31   luster and white streak. The Mohs hardness is ~3½-4; the tenacity is brittle,

32   the fracture is irregular, and indistinct cleavage was observed on {001}.

33   Electron microprobe analyses provided the empirical formula

34     $Pb_{4.97}(PO_4)_3(OH_{0.69}F_{0.33}Cl_{0.06})_{\sum 1.08}$. The calculated density using the measured

35   composition is 7.32 g·cm^{-3}. Powder X-ray diffraction data for the type

36   material is compared to data previously reported for hydroxylpyromorphite

37   from the talc mine at Rabenwald, Austria, and from Whytes Cleuch,

38   Wanlockhead, Scotland. Hydroxylpyrmorphite is hexagonal, $P6_3/m$, at 100K,

39     $a = 9.7872(14)$, $c = 7.3070(10)$ Å, $V = 606.16(19)$ Å^3, and $Z = 2$. The structure

40   ($R_1 = 0.0181$ for 494 $F > 4\sigma(F)$ reflections) reveals that hydroxylpyromorphite

41   adopts a column anion arrangement distinct from other members of the apatite

42   supergroup due to the presence of fluorine and steric constraints imposed by

43   stereoactive lone-pair electrons of Pb^{2+} cations. The F$^-$ anion sites are

44   displaced slightly from hydroxyl oxygen anions, which allows for stronger

45   hydrogen-bonding interactions that may in turn stabilize the observed column-

46   anion arrangement and overall structure. Our modern characterization of

47   hydroxylpyromorphite provides deeper understanding to a mineral useful for

48   remediation of lead-contaminated water.

49

50   **Keywords:** Hydroxylpyromorphite; apatite; crystal structure; Copps mine;

51   infrared spectroscopy; Michigan; anion column

52

53   **Introduction**

54   The apatite supergroup comprises a series of structurally related

55   minerals with the general formula $^{IX}M1_2{}^{VII}M2_3(^{IV}TO_4)_3X$ based upon a

56   heteropolyhedral framework of metallic (M = Ca^{2+}, Pb^{2+}, Cd^{2+}, Ba^{2+}, Sr^{2+},

57   Mn^{2+}, Na^+, Ce^{3+}, La^{3+}, Y^{3+}, Bi^{3+}) and tetrahedral cations (T = P^{5+}, V^{5+}, As^{5+},

58   Si^{4+}, S^{6+}, B^{3+}) with columns containing the X anions: F$^-$, (OH)$^-$, or Cl$^-$ (Pasero

59   et al., 2010). More than fifty years of crystallographic studies of

60   mineralogical, biological and synthetic apatite phases have revealed that

61   extensive anion solid solution occurs among the group members and that

62   certain species exhibit specific anion-column ordering schemes dependent on

63   size, site occupancy, and the chemical makeup of the anion column (Hughes

64   and Rakovan, 2015; White and ZhiLi, 2003). Our understanding of anion-

65   column ordering in the calcium phosphate apatites is now rather well-

66   established based on several studies of natural and synthetic samples (Hughes

67   et al., 2014, 2016, 2018; Kelly et al., 2017), however, details of anion ordering

68   in the pyromorphite group are incomplete due to missing data for the fluor and

69   hydroxyl members.

70   In existing literature, numerous references have been made to

71   "hydroxypyromorphite, hydroxopyromorphite, lead apatite, or lead

72   hydroxypatite" compounds as both synthetic and natural material, although

73   until now the crystal structure of hydroxylpyromorphite found in Nature was

74   not determined, nor formally considered a mineral (Brückner et al., 1995;

75   Cockbain, 1968; Lower et al., 1998; Mavropoulos et al., 2002; Zhu et al.,

76   2016). Here for the first time, we provide a full structural analysis of the

77   mineral hydroxylpyromorphite.

78   The mineral and its name have been approved by the Commission on

79   New Minerals, Nomenclature and Classification of the International

80   Mineralogical Association (IMA2017-075). The prefix "hydroxyl" is used in

81   accordance with the nomenclature scheme for the apatite supergroup (Hatert et

82   al., 2013; Pasero et al., 2010). The description is based on one holotype

83   specimen deposited in the collections of the Natural History Museum of Los

84   Angeles County, 900 Exposition Boulevard, Los Angeles, CA 90007, USA,

85   catalogue number 66627.

86   **Occurrence**

87   Hydroxylpyromorphite crystals were collected by Shawn M. Carlson

88   and one of the authors (CL) in 2015 at the Copps mine, Gogebic County,

89   Michigan. This "mine" is actually a late 19th century test exploration

90   consisting of approximately eleven small adits, pits, trenches, and shafts

91   spanning a distance of about 225 meters, and located in sections 14, 15, and

92   22, T47N, R43W (Carlson et al., 2017). The exploration tested discontinuous

93   and sub-economic precious and base-metal mineralization, mainly Pb, Cu, and

94   Ag contained within the Early Proterozoic Copps Formation (Baraga Group of

95   the Marquette Range Supergroup), a formation comprised primarily of

96   metagraywacke and conglomeratic, ferruginous quartzite (Klasner et al.,

97   1998). Hydroxylpyromorphite has so far been identified from a single

98   specimen of vein quartz and its only intimate association is with quartz as vug

99   linings, but more generally is associated with twenty-one minerals, one

100   mineraloid, and seven unknowns that have been documented at the prospect.

101   The identified minerals include: anglesite, beaverite-(Cu), calcite, cerussite,

102   chalcopyrite, chamosite, corkite, covellite, dolomite, galena, goethite, gypsum,

103   hematite, jarosite, "K-feldspar", malachite, plumbojarosite, pyrite, quartz,

104   "sericite", and sphalerite (Carlson *et al.*, 2017). The morphology and

105   association of hydroxylpyromorphite suggest that it is a geogenic secondary

106   Pb phase and is not post-mining in origin.

107   In what may be the first report of natural hydroxylpyromorphite,

108   Temple (1956) identified a lead phosphate mineral from an unspecified vein at

4

109   Whytes Cleuch, Wanlockhead, Dumfries & Galloway, Scotland, UK, which

110   he described as "lead hydroxyapatite," but provided no chemical data. In

111   Temple's words, "The mineral appears to represent a further substitution in

112   the pyromorphite group, the hydroxyl group substituting for chloride." It

113   forms powdery white coatings associated with *polysphaerite*

114   [phosphohedyphane, $Ca_2Pb_3(PO_4)_3Cl$], as pseudomorphs after galena. We

115   have sought and tested similar material from Whytes Cleuch; however, in the

116   single specimen studied we have only identified phosphohedyphane and

117   anglesite. Single crystals of hydroxylpyromorphite, if present, were too

118   intimately admixed with phosphohedyphane and far too small for conventional

119   single-crystal X-ray diffraction (SCXRD) analysis. This was likewise the case

120   for material from a third reported occurrence of thin white coatings of finely

121   crystalline hydroxylpyromorphite from the talc mine at Rabenwald, Anger,

122   Weiz, Styria, Austria (Kolitsch and Lóránth 2016). According to the website

123   Mindat.org (accessed July 2020), several other reported hydroxylpyromorphite

124   occurrences exist, but we have not been able to confirm their validity. Two

125   samples tested from the Motel 22 occurrence, Brady Township, Huntingdon

126   Co., Pennsylvania, USA, were found to contain only anglesite and cerussite.

127   An additional occurrence of anthropogenic "hydroxylpyromorphite" is

128   reported by Kirchner along with other secondary Pb, Cu, and As minerals on

129   medieval slag heaps south of Radhausberg, Austria (Kirchner et al., 2007).

130   Our difficulty locating suitable material for single-crystal structure

131   determination may attest to why the mineral has remained undescribed until

132   now; however, we are able to provide a comparison of X-ray powder

133   diffraction data for Copps mine crystals to the original "lead hydroxyapatite"

134   data given by Temple (1954), and hydroxylpyromorphite from Kolitsch and

135   Lóránth (2016). While we acknowledge that the Copps mine is not the first

136   reported occurrence for hydroxylpyromorphite, it is the first to provide

137   suitable material for a full description of the phase.

138   **Physical and optical properties**

139   On the holotype specimen, hydroxylpyromorphite crystals are arranged

140   in aggregates of randomly oriented colorless hexagonal prisms, primarily

141   between about 20 – 35 μm in length and 6 – 10 μm in diameter (Fig.

142   1), although several highly-elongated crystals reaching 250 μm in length were

143   also found. Crystals exhibit the {100} prism and are terminated by the {101}

144   pyramid (Fig. 2). They are translucent with a vitreous luster, have a white

145   streak and are non-fluorescent under both long- and short-wave ultraviolet

146   illumination. The crystals are brittle with indistinct {001} cleavage and

147   irregular fracture. The Mohs hardness is about 3.5-4 based on scratch tests.

148   The density could not be measured due to the limited availability of material

149   and because it exceeds that of available heavy liquids. The calculated density

150   is 7.32 g·cm^{-3} based on the empirical formula and 7.33 g·cm^{-3} for the ideal

151   formula.

152   Optically, hydroxylpyromorphite is uniaxial (-), with ω - ε

153   birefringence = 0.03. The small crystal size and high indices of refraction

154   made the measurement of indices of refraction impractical. The predicted

155   average index of refraction based upon the Gladstone-Dale relationship is

156   2.04. The indices of refraction of pyromorphite are slightly higher by

157   comparison, ω = 2.058, ε = 2.048 (Anthony et al., 2000).

158   **Infrared Spectroscopy**

6

159   Attenuated total reflectance (ATR) Fourier-transform infrared (FTIR)

160   spectra were obtained using a liquid N_2-cooled SENSIR Technologies

161   IlluminatIR mounted to an Olympus BX51 microscope. A ContactIR ATR

162   objective (diamond and ZnSe lens) was pressed into crystals of

163   hydroxylpyromorphite and spectra were measured from 4000 to 650 cm^{-1}. The

164   infrared spectrum is shown in Figure 3. Broad hydroxyl stretching vibrations

165   occur between ~3600 and 3000 cm^{-1}. Approximate O-H$\cdots$O hydrogen bond-

166   lengths calculated from the observed stretching frequencies lie within the

167   range ~3.2 to 2.7 Å using the correlation function given by Libowitzky (1999).

168   Hydrogen-bonding interactions in the crystal structure are weak ($\geq$ 3 Å), and

169   thus stronger H-bonding interactions observed in the IR spectrum may be

170   attributable to adsorbed H_2O (Ishikawa et al., 1989). A broad and weak band

171   centered near ~1950 cm^{-1} is likely a combination band (ν_3 PO4 + ν_1 PO$_4$). The

172   ν_3 anti-symmetric stretching mode of PO$_4$ units occurs as moderately strong

173   bands at 1053 and 1000 cm^{-1}. The ν_1 PO$_4$ symmetric stretching mode is found

174   as a very strong band at 917 cm^{-1}, and the weak ν_4 bending mode of PO$_4$

175   occurs at 764 cm^{-1}.

176
177   **Chemical composition**

178   Chemical analyses (12) were performed using a JEOL JXA-773

179   electron microprobe operating at an accelerating voltage of 15 kV, with a

180   beam current of 10 nA and 10 μm spot diameter. Crystals were oriented and

181   analyzed using surfaces perpendicular to the *c* axis (see below).

182   Hydroxylpyromorphite contains major Pb, P and O, with minor F and trace Cl.

183   No other elements were detected. Matrix effects were accounted for using the

7

184   ZAF correction routine (Armstrong, 1988). Due to the limited amount of

185   material available, the H_2O content was not measured and is instead calculated

186   by stoichiometry with respect to the structure. Analytical data are given in

187   Table 1. The empirical formula, calculated on the basis of 3 P atoms per

188   formula unit (*apfu*) is $Pb_{4.97}(PO_4)_3(OH_{0.69}F_{0.33}Cl_{0.06})_{\Sigma 1.08}$. The ideal formula is

189    $Pb_5(PO_4)_3(OH)$, which requires PbO 83.41, P_2O_5 15.91, H_2O 0.67, total 100

190   wt%.

191   Electron-beam induced halogen migration is commonly observed in

192   fluorapatites and chlorapatites (Stock et al., 2015), where an inaccurate

193   measured halogen concentration is caused by accumulation of those elements

194   near the analysis surface. Migration is most pronounced when the electron

195   beam impinges on (001) sections, parallel to the anion columns in the apatite

196   structure, whereas minimal migration occurs in {100} sections, that is, when

197   the beam is normal to the *c* axis (Stormer et al., 1993). After prolonged

198   exposure to the electron beam, a decrease of measured signals attributed to F

199   and Cl corresponds to loss due to volatility. We conducted a series of

200   microprobe experiments using hydroxylpyromorphite crystals with their *c* axis

201   oriented parallel to the beam to monitor anion migration. Raw counts for F in

202   hydroxylpyromorphite were collected using sequential 5 second count times

203   up to 2 minutes at 15 kV, 25 nA, and 1 µm beam diameter. No statistically

204   significant change in the F signal over the period of two minutes was

205   observed, suggesting that significant electron-beam induced F migration does

206   not occur, at least on this time scale (Fig. S1). The very small size of the

207   polished crystal sections (~5 µm) and low total F and Cl content may also lead

208   to poor resolution of halogen migration here.

209   An additional single spot analysis was noted to display anomalously

210   high F content, 1.02 wt%, corresponding to the empirical formula

211     $Pb_{5.23}(PO_4)_3(F_{0.76}OH_{0.21}Cl_{0.08})_{\Sigma1.04}$. This single analysis may correspond to the

212   yet undescribed F-analogue of pyromorphite, "fluorpyromorphite," but was

213   considered to be of low quality due to the high proportion of Pb:P. Subsequent

214   analyses have not revealed demonstrably F-dominant crystals, nor have we

215   observed any clear zonation of F content within the resolution of the

216   microprobe that might suggest the F-dominant analogue exists at the Copps

217   mine.

218

219   **Powder X-ray diffraction**

220   X-ray powder diffraction data were obtained using a Rigaku R-Axis

221   Rapid II curved imaging plate microdiffractometer with monochromatized

222   Mo$K\alpha$ radiation. A Gandolfi-like motion on the φ and ω axes was used to

223   randomize diffraction from the sample. Observed d-values and intensities

224   were derived by profile fitting using JADE 2010 software (Materials Data,

225   Inc.). Data (in Å for Mo$K\alpha$) are given in Table S1. Unit-cell parameters

226   refined from the powder data using JADE 2010 with whole pattern fitting in

227   space group $P6_3/m$ are: $a = 9.7858(14)$ Å, $c = 7.3072(11)$ Å, $V = 606.0(2)$ Å^3.

228   The powder X-ray diffraction data for Copps mine

229   hydroxylpyromorphite presented here agrees favorably with the lines observed

230   by Temple (1954) for "lead hydroxyapatite" from Whytes Cleuch and

231   synthetic material listed by Hey (1950), as well as with data measured for

232   hydroxylpyromorphite from the talc mine at Rabenwald, Austria (Uwe

233   Kolitsch pers. comm.; Table 2).

Single-crystal X-ray diffraction

234

235   A small elongated hexagonal prism was chosen for the single-crystal

236   X-ray diffraction experiment. Data were collected at 100 K using

237   monochromatized Mo$K\alpha$ X-rays from a microfocus source and an Apex II

238   CCD-based detector mounted to a Bruker Apex II Quazar three-circle

239   diffractometer. Reflections were integrated and corrected for Lorentz,

240   polarization, and background effects using the Bruker program SAINT. A

241   multi-scan semi-empirical absorption correction was applied using equivalent

242   reflections in SADABS-2012 (Krause et al., 2015). An initial structure model

243   was obtained by the charge-flipping method using SHELXT (Sheldrick,

244   2015a) in space group $P6_3/m$, and refinements were made by full-matrix least-

245   squares on F^2 using SHELXL-2016 (Sheldrick, 2015b). All atoms except

246   those in the anion column were refined with anisotropic displacement

247   parameters, and the U_{eq} of atom H1 set to 1.2 times that of its donor O atom,

248   O4. The data collection and refinement information are presented in Table S2,

249   atomic coordinates and displacement parameters in Table S3, selected bond

250   distances in Table S4, and a bond-valence analysis in Table S5.

251

Features of the Crystal Structure

252

253   The crystal structure is a heteropolyhedral framework consisting of

254   PbO_9 and $PbO_6(OH)_2$ polyhedra and phosphate (PO_4) tetrahedra arranged into

255   the well-known apatite-type structure (Fig. 4). Hexamers of Pb2-centered

256   polyhedra share a central atom O4 located on (0,0,0), the oxygen atom of the

257   hydroxyl anion, forming columnar units that extend along [001]. A second

258   structural unit built from Pb1-centered polyhedra consists of simple chains

259   that extend along [001] and connect three sets of hexamers such that six chains

260   adorn each column of hexamers. Phosphate tetrahedra decorate the chains and

261   columns that connect the Pb polyhedra as well as the hexamer columns to

262   chains.

263   The P atom position in hydroxylpyromorphite is coordinated by four

264   oxygen atoms in a tetrahedral arrangement and the average P–O bond distance

265   is 1.544 Å with little variance (Table S4). The coordination environment of

266   atom Pb1 takes the shape of a tricapped trigonal prism by bonding to nine

267   phosphate O atoms with an average bond distance of 2.703 Å. Three of the

268   nine bonds to Pb1 are short with O2 at 2.512 Å, with three additional long

269   bonds to O1 at 2.724 Å, and three to O3 at 2.873 Å. The large bond length

270   variance and *cis* coordination of the short Pb1-O bonds indicates a

271   stereochemically active $6s^2$ lone pair of electrons, which due to symmetry

272   constraints, necessitates their placement along the three-fold rotation axis

273   between pairs of Pb1 atoms and directed towards the pyramidal void space

274   formed by O1 or O2 atoms (Dai et al., 1991). The lone pair may reside

275   predominantly in the larger void formed by O1 atoms, with a void volume

276   measuring ~30 $Å^3$, rather than that formed by O2 atoms, with a slightly

277   smaller, ~23 $Å^3$ void. Furthermore, at 3.694(1) Å, the Pb1–Pb1 distance

278   through the O1 triangle is ~0.08 Å longer than the Pb1–Pb1 distance through

279   the O2 triangle, supporting dominant occupancy of the lone-pair within the O1

280   void.

281   Atom Pb2 forms six bonds with O atoms of phosphate groups and two

282   hydroxyl oxygen atoms (O4) in the column, giving an eight-coordinated

283   irregular polyhedron with a <Pb2–O> bond distance of 2.707 Å. These bonds

284   also exhibit variable length with lopsided long and short bonds provoked by

285    $6s^2$ lone-pair electrons, and includes a short 2.398 Å bond to O1 and four

286   relatively short bonds to O3, with two at 2.595 Å and two at 2.637 Å. The

287   long bond to O2 at 2.930 Å and two long bonds with O4 at 2.932 Å

288   accommodate space for the lone-pair electrons. Based on symmetry

289   constraints, the Pb2 lone-pair electrons are directed inward and adjacent to the

290   column anions along the $z = \frac{1}{4}$ mirror plane. Their placement imposes several

291   restrictions on the anion column arrangement in hydroxylpyromorphite.

292   The anisotropic displacement parameters of atom Pb1 are essentially

293   isotropic in shape, however, atom Pb2 exhibits a three-fold greater elongation

294   along the c axis/U^{33} vector (0.035 Å^2) relative to Pb1 (0.012 Å^2). The apparent

295   positional disorder is not significant enough to consider splitting of the Pb1

296   position, though could suggest a long-range averaged displacement due to

297   inhomogeneous column anion arrangements. We cannot, however, discount

298   that the effect may be due to an inadequate absorption correction.

299

300   **Anion Column Ordering**

301   The chemical analyses indicate that hydroxylpyromorphite from the

302   Copps mine contains appreciable fluoride (0.33 *apfu*) and this raises a

303   question regarding its position amongst OH groups in the anion column. The

304   hydroxyl oxygen atom O4 exhibited signs of site splitting and a weak Fourier

305   difference density peak (~1 e/A^3) was located approximately ~0.7 Å from O4.

306   Site scattering refinement trials attempted with full H atom occupancy at this

307   peak led to anomalously high displacement parameters and excessive

308   occupancy (>1) of H, as expected for the occupation of a heavier atom, and we

309   proceeded with refinement of this peak as a partially occupied F atom.

310   Attempts to refine the disorder as a mixed occupancy site containing both F

311   and H were unsuccessful, so the calculated site-scattering from the chemical

312   analyses for F and H, 3.66 *epfu*, was initially used to guide the disorder

313   refinement with a split-site model containing separate F and H atom sites. In

314   the final iterations, their occupancies and positions were allowed to refine

315   freely.

316   Overlap of the column anions and steric limitations imposed by Pb2

317   lone-pair electrons necessitates specific anion-occupancy considerations based

318   on symmetry constraints, resulting in several possible local configurations of

319   anions (Fig. 5). Related through hexagonal symmetry, the F$^-$ anions in

320   hydroxylpyromorphite may substitute locally at column anion sites allowing

321   for reversal of the hydrogen-bonding sequence (Fig. 5B). In this case, F

322   occupancy (which requires local O4 vacancy) results in stronger hydrogen-

323   bonding interactions within the column with a F–O distance of 3.02 Å.

324   Hydrogen-bonding interactions in end-member hydroxylpyromorphite are

325   otherwise non-existent, with O4–O4 donor-acceptor distances measuring >3.6

326   Å. Thus, unique F sites displaced slightly from O sites in

327   hydroxylpyromorphite may provide for a more stable anion column

328   arrangement through stronger hydrogen-bonding interactions, potentially

329   yielding a more stable structure with respect to end-member fluor- or

330   hydroxylpyromorphite.

331   Anion column ordering in fluor-, chlor-, and hydroxylapatites has been

332   investigated in depth by others (Hughes et al., 1989, 2014, 2016, 2018; Kelly

333   et al., 2017) and these studies have provided detailed ordering schemes based

334   on steric limitations of the column and anion constituents. In apatite

335   containing roughly equivalent amounts of F and OH, distinct F and OH sites

336   are found and their ionic radii [F 1.30 Å and O 1.31 Å (Shannon and Prewitt,

337   1969)] permit each site to be occupied simultaneously, with occupancy and

338   ordering considerations. As a result, complete solid solution between binary F-

339   OH apatite exists with end-member defining F and OH sites while maintaining

340   $P6_3/m$ symmetry (Hughes et al., 1989). However, the presence of minor Cl in

341   fluor- and hydroxylapatite can lead to splitting of the Ca2 site to accommodate

342   the large Cl anions (Sudarsanan and Young, 1978). No such Pb2-site splitting

343   is observed in hydroxylpyromorphite, where the Pb–F bond distance measures

344   2.58(4) Å, considerably shorter but more ideal than those found in synthetic

345   lead-fluorapatite and Sr-substituted lead-fluorapatite, where Pb/Sr–F bond

346   distances range from ~2.75 to 2.95 Å (Badraoui et al., 2006; Fleet et al.,

347   2010). The Pb–F bond distance in fluorphosphohedyphane is 2.87 Å (Kampf

348   and Housley, 2011). Bond-valence analysis of hydroxylpyromorphite indicates

349   that the refined configuration provides ideal sums for all constituents except F

350   at 0.75 *vu*, not accounting for partial occupancy or hydrogen bonding [~0.17

351   vu] (Table S5). This is more favourable than sums incident to F in

352   fluorphosphohedyphane, 0.594 *vu*, and synthetic $Pb_5(PO_4)_3F$, 0.593 *vu* (Kampf

353   and Housley, 2011).

354   Hughes et al. (2014, 2016, 2018) and Kelly et al. (2017) found the use

355   of isotropic displacement parameters necessary to describe the anion column

356   positions in tertiary and binary hydroxyl-, fluor-, and chlorapatites. This is an

357   effect of the significant anion disorder and Ca site splitting observed in fluor-

358   and hydroxylapatite crystals containing Cl, which due to steric constraints,

359 require introduction of split Cl sites and mixed occupancy O-Cl sites (Fig. 6).

360 We observe similar O-Cl site mixing in hydroxylpyromorphite due to the

361 steric limitations of lone-pair electrons and the formation of an otherwise

362 unfavourably short Pb–Cl bond at ~2.58 Å. Thus, at least two column-anion

363 sites are found in hydroxylpyromorphite; including an O/Cl site at $z = 0$ and a

364 F site at $z = 0.087$. Such positioning is comparable to the Cl sites found in

365 chlorapatite, mimetite, pyromorphite, alforsite, pieczkaite, and turneaureite,

366 that sit on analogous $2b$ Wyckoff positions (0,0,0).

367

368 **Relation to synthetic phases**

369 Synthetic hydroxylpyromorphite was prepared by Barinova et al.

370 (1998) using hydrothermal methods (260 °C, 100 atm) and its measured

371 single-crystal unit-cell parameters are nearly identical to crystals from the

372 Copps mine (Table 3). Notable structural differences include slightly larger

373 separation between Pb2-Pb2 pairs and longer Pb2–OH bond distances in

374 natural hydroxylpyromorphite; which is likely a response of lone-pair

375 electrons to the presence of minor F and trace Cl that is absent in the synthetic

376 crystals. Barinova et al. (1998) refined the O of the hydroxyl group at the $2b$

377 Wyckoff position ($z = 0$), in agreement with our description. In contrast, the O

378 of the hydroxyl in the structure refined by Brückner et al. (1995) from powder

379 X-ray diffraction data is displaced slightly from the origin, at $z = 0.04$. Their

380 model was refined based on starting coordinates from a lead-substituted

381 hydroxyapatite with approximately 80% Pb content, determined by Bigi et al.

382 (1989). The refinements show clearly that the O atom site of the hydroxyl

383 anion is strongly correlated with Pb content and that with increasing Pb

384   substitution, the O site moves further from the mirror plane and Pb/Ca

385   triangle, shifting closer to $z = 0$. This suggests that a solid solution series may

386   extend between hydroxylpyromorphite and the yet undescribed mineral

387   "hydroxylphosphohedyphane," $Ca_2Pb_3(PO_4)_3(OH)$.

388   In the structure of synthetic fluorpyromorphite, Belokoneva et al.

389   (1982) found that F^- anions assumed a position at $z = 0.25$, in plane with the

390   triangle of Pb atoms, forming a very short bond with Pb2 of 2.33 Å (1.52 vu).

391   In the neutron powder diffraction study by Kim et al. (1997), F atoms sit at $z =$

392   0.5/0. It was later shown by Badraoui et al. (2006) using X-ray Rietveld

393   refinement and by Fleet et al. (2010) using single-crystal X-ray diffraction that

394   the F site adopts a split atom position at $z = 0.449$ and 0.461, with 50/50

395   occupancy. This is in agreement with our findings for hydroxylpyromorphite,

396   where F anions are displaced slightly from O atoms of hydroxyl anions.

397   White and ZhiLi (2003) examined the influence of stereoactive lone-

398   pair electrons on symmetry and metaprism twist angles in apatites and related

399   structures. Likewise, Baikie et al. (2014) compile both new and old structure

400   data for several natural lead-containing apatites as a function of temperature,

401   revealing that the twist angle of opposing triangular faces of the framework

402    $Pb1O_6$ metaprism projected on (001) is sensitive to the anion and tetrahedral

403   cation content. These studies show that metaprism twist angle is inversely

404   related to the cross section of the anionic column and the average effective

405   ionic radius, and that the twist angle contracts significantly at lower

406   temperatures. Metaprism twist angles of selected synthetic hydroxl- and

407   fluorpyromorphites are compared in Table 3. The Pb1 metaprism twist in

408   hydroxylpyromorphite is the smallest angle of those calculated using the

409   method of White and ZhiLi (2003), likely due to the low temperature used for

410   data collection. However, considering the large range of twist angles observed

411   for synthetic hydroxyl- and fluorpyromorphites, it may be interesting to test

412   the influence of variable OH⁻, F⁻, Pb, and Ca content on anion ordering and

413   metaprism twist angle.

414   Because of their essentially identical X-ray scattering factors, it is

415   possible that the refined O and F column anion sites in hydroxylpyromorphite

416   can contain either anion; however, full occupancy of the $z = 0$ position by O

417   defines the end-member species. Our inability to distinguish O and F by site

418   scattering does not affect our analysis of the anion ordering except for the

419   location of the hydroxyl H atom, which for F at $z = 0$ and O at $z = 0.087$ would

420   either occur near $z = \sim0.23$ or ~0.05. The corresponding donor-acceptor

421   distances for this configuration become very long, > 3.6 Å for H at $z = 0.23$, or

422   very short, ~2.4 Å ($z = 0.05$), and may account for the relatively strong

423   hydrogen-bonding interactions (~2.7 Å) observed in the infrared spectrum.

424   Although no electron density was observed for $z > 0.14$, diffraction

425   contributions of H atoms to the disorder may not be significant or are obscured

426   in the presence of heavier scattering atoms. Additional synthetic studies are

427   needed to better understand the effects of Cl, F, and OH content on anion-

428   column ordering and hydrogen-bonding in tertiary pyromorphites; however,

429   our findings for fluoride-rich hydroxylpyromorphite suggest that solid solution

430   between the yet undescribed mineral "fluorpyromorphite" and

431   hydroxylpyromorphite is possible.

432

433   **Implications**

434   Consumption of lead-contaminated water can lead to serious health

435   problems, especially in children, and there is currently no tolerable level of

436   lead exposure identified by the U.S. Centers for Disease Control and

437   Prevention (CDC, 2013). In like manner, the Environmental Protection

438   Agency uses a "maximum contaminant level goal" of zero for Pb (USEPA,

439   2019). Rather than an acceptable minimum contaminant level as used for other

440   contaminants, there are treatment regulations in place when "action-level"

441   (0.015 mg/L) lead concentrations are reached. When concentrations above the

442   action level are found, the so-called Lead and Copper Rule is applied,

443   whereby municipal water plants introduce corrosion control by adjusting pH,

444   lowering dissolved carbonate content, and adjusting the Cl^-/SO_4^{2-} ratio with

445   the coagulants ferric chloride or ferric sulfate (USEPA, 2019; Nguyen et al.,

446   2011). These treatments reduce the corrosion rate of pipes and leaded solder

447   joints, lowering Pb levels at the tap; however, treatment of the source water

448   itself is at times necessary in aquifers with high levels of Pb or other

449   contaminants. One of the most commonly applied methods for direct removal

450   of Pb is the addition of phosphoric acid. When added to Pb-contaminated

451   water, phosphoric acid will initially cause precipitation of

452   hydroxylpyromorphite due to its significantly lower solubility than

453   hydroxylapatite, $K_{sp} = \sim 10^{-81}$ vs $\sim 10^{-58}$ (Zhu et al., 2016); and indeed,

454   hydroxylpyromorphite was identified as a corrosion product of lead pipes in

455   laboratory experiments (Grimes et al., 1995) and within the city of Glasgow,

456   Scotland, UK, municipal water supply (Peters et al., 1999).

457   In practice, higher concentrations of Ca, Cl, and F in drinking water

458   may lead to precipitation of mixed-anion and dominantly Ca- and Cl-bearing

18

459   apatite phases that incorporate trace Pb depending on the local chemistry.

460   However, Pb was efficiently immobilized in contaminated soils mixed with

461   finely ground fluorapatite-bearing rocks in experiments by Ma et al. (1995),

462   who observed that the primary mechanism of Pb immobilization was

463   precipitation of a "fluoropyromorphite"-like mineral. Likewise, experiments

464   by Valsami-Jones et al. (1998) and Mavropoulos et al. (2002) reveal that

465   release of Pb from less soluble apatite phases can occur by slow diffusion,

466   with re-uptake into newly precipitated hydroxylpyromorphite layers occurring

467   on their surfaces.

468   Our investigations of hydroxlpyromorphite suggest solid solution is

469   possible between it and other apatite-supergroup members, specifically the

470   undescribed minerals "fluorpyromorphite" and "hydroxylphosphohedyphane,"

471   but further work is needed to understand how excess chloride may affect the

472   anion-column arrangement and hydrogen bonding for binary (F-Cl, OH-Cl, F-

473   OH) or tertiary (F-Cl-OH) substitutions. The full description of

474   hydroxylpyromorphite presented here may inspire future synthetic studies to

475   provide a deeper understanding of the relationship between anion-column

476   ordering and resultant properties, such as solubility, reactivity, and Pb

477   mobility in complex systems. This information could help optimize

478   remediation and corrosion control for a wider variety of Pb-contaminated

479   aquifers and soils.

480

481   **Acknowledgements**

References

Anthony, J.W., Bideaux, R.A., Bladh, K.W., and Nichols, M.C. (2000) Handbook of Mineralogy. Mineral Data Publishing, Tucson, AZ, USA.

Armstrong, J.T. (1988) Quantitative analysis of silicates and oxide minerals: Comparison of Monte-Carlo, ZAF and Phi-Rho-Z procedures In D.E. Newbury, Ed. Microbeam Analysis San Francisco Press, Inc., San Francisco, CA.

Badraoui, B., Aissa, A., Bigi, A., Debbabi, M., and Gazzano, M. (2006) Structural investigations of lead–strontium fluoroapatites. Journal of Solid State Chemistry, 179, 3065–3072.

Baikie, T., Schreyer, M., Wei, F., Herrin, J.S., Ferraris, C., Brink, F., Topolska, J., Piltz, R.O., Price, J., and White, T.J. (2014) The influence of stereochemically active lone-pair electrons on crystal symmetry and twist angles in lead apatite-2H type structures. Mineralogical Magazine, 78, 325–345.

Barinova, A.V., Bonin, M., Pushcharovskii, D.Y., Rastsvetaeva, R.K., Schenk, K., and Dimitrova, O.V. (1998) Crystal structure of synthetic hydroxylpyromorphite $Pb_5(PO_4)_3(OH)$. Crystallography Reports, 43, 189–192.

Belokoneva, E.L., Troneva, E.A., Dem'yanets, L.N., Duderov, N.G., and Belov, N.V. (1982) Crystal structure of synthetic fluoropyromorphite $Pb_5(PO_4)_3F$. Kristallografiya, 27, 793–794 (In Russian).

Bigi, A., Ripamonti, A., Brückner, S., Gazzano, M., Roveri, N., and Thomas, S.A. (1989) Structure refinements of lead-substituted calcium hydroxyapatite by X-ray powder fitting. Acta Crystallographica, B45, 247–251.

Brückner, S., Lusvardi, G., Menabue, L., and Saladini, M. (1995) Crystal structure of lead hydroxyapatite from powder X-ray diffraction data. Inorganica Chimica Acta, 236, 209–212.

Carlson, S.M., Laughlin-Yurs, C., Olds, T.A., Fountain, D.R., and Mills, O.P. (2017) Secondary Lead Minerals from the Copps Mine, Gogebic County, Michigan. Rocks & Minerals, 92, 166–171.

Centers for Disease Control and Prevention (CDC). (2013, April 5) Blood lead levels in children aged 1-5 Years - United States, 1999-2010. MMWR, Morbidity and Mortality Weekly Reports, 62, 245–248.

Cockbain, A.G. (1968) Lead apatite solid-solution series. Mineralogical Magazine and Journal of the Mineralogical Society, 36, 1171–1173.

Dai, Y., and Hughes, J. (1989) Crystal-Structure Refinements of Vanadinite and Pyromorphite. Canadian Mineralogist, 27, 189–192.

Dai, Y., Hughes, J.M., and Moore, P.B. (1991) The crystal structures of mimetite and clinomimetite, $Pb_5(AsO_4)_3Cl$. Canadian Mineralogist, 29, 369–376.

Fleet, M.E., Liu, X., and Shieh, S.R. (2010) Structural change in lead fluorapatite at high pressure. Physics and Chemistry of Minerals, 37, 1–9.

Grimes, S.M., Johnston, S.R., and Batchelder, D.N. (1995) Lead carbonate–phosphate system: solid–dilute solution exchange reactions in aqueous systems. Analyst, 120, 2741–2746.

541 Hatert, F., Mills, S.J., Pasero, M., and Williams, P.A. (2013) CNMNC
542   guidelines for the use of suffixes and prefixes in mineral
543   nomenclature, and for the preservation of historical names. European
544   Journal of Mineralogy, 25, 113–115.
545 Hey, M.H. (1950) An index of mineral species & varieties arranged
546   chemically, with an alphabetical index of accepted mineral names
547   and synonyms. 608 p. Printed by order of the Trustees of the British
548   Museum, London.
549 Hughes, J.M., Cameron, M., and Crowley, K.D. (1989) Structural variations
550   in natural F, OH, and Cl apatites. American Mineralogist, 74, 870–
551   876.
552 Hughes, J.M., Harlov, D., Kelly, S.R., Rakovan, J., and Wilke, M. (2016)
553   Solid solution in the apatite OH-Cl binary system: Compositional
554   dependence of solid-solution mechanisms in calcium phosphate
555   apatites along the Cl-OH binary. American Mineralogist, 101, 1783–
556   1791.
557 Hughes, J.M., Harlov, D., and Rakovan, J.F. (2018) Structural variations
558   along the apatite F-OH join. American Mineralogist, 103, 1981–
559   1987.
560 Hughes, J.M., Nekvasil, H., Ustunisik, G., Lindsley, D.H., Coraor, A.E.,
561   Vaughn, J., Phillips, B.L., McCubbin, F.M., and Woerner, W.R.
562   (2014) Solid solution in the fluorapatite-chlorapatite binary system:
563   High-precision crystal structure refinements of synthetic F-Cl apatite.
564   American Mineralogist, 99, 369–376.
565 Hughes, J.M., and Rakovan, J.F. (2015) Structurally Robust, Chemically
566   Diverse: Apatite and Apatite Supergroup Minerals. Elements, 11,
567   165–170.
568 Ishikawa, T., Wakamura, M., and Kondo, S. (1989) Surface characterization
569   of calcium hydroxylapatite by Fourier transform infrared
570   spectroscopy. Langmuir, 5, 140–144.
571 Kampf, A.R., and Housley, R.M. (2011) Fluorphosphohedyphane,
572   Ca2Pb3(PO4)3F, the first apatite supergroup mineral with essential
573   Pb and F. American Mineralogist, 96, 423–429.
574 Kelly, S.R., Rakovan, J., and Hughes, J.M. (2017) Column anion
575   arrangements in chemically zoned ternary chlorapatite and
576   fluorapatite from Kurokura, Japan. American Mineralogist, 102, 720–
577   727.
578 Kim, J.Y., Hunter, B.A., Fenton, R.R., and Kennedy, B.J. (1997) Neutron
579   powder diffraction study of lead hydroxyapatite. Australian Journal
580   of Chemistry, 50, 1061–1065.
581 Kirchner, E.C., Mrazek, R., and Wimmer, H. (2007) Neue Mineralfunde von
582   Bergbauhalden Radhausberg Süd (Weißental) Kreuzkogel.
583   Mineralogisches Archiv Salzburg, 12, 251–254 (In German).
584 Klasner, J.S., LaBerge, G.L., and Cannon, W.F. (1998) Geologic map of the
585   eastern Gogebic iron range, Gogebic County, Michigan. IMAP 2606
586   (Online). Available: https://pubs.er.usgs.gov/publication/i2606
587   (accessed July 18, 2020).
588 Kolitsch, U., and Lóránth, C. (2016) Descloizit und das Hydroxyl-Analogon
589   von Pyromorphit vom Talkbergbau Rabenwald bei Anger. Der
590   Steirische Mineralog, 31, 52.

591   Krause, L., Herbst-Irmer, R., Sheldrick, G.M., and Stalke, D. (2015)
592   Comparison of silver and molybdenum microfocus X-ray sources for
593   single-crystal structure determination. Journal of Applied
594   Crystallography, 48, 3–10.
595   Libowitzky, E. (1999) Correlation of O-H stretching frequencies and O-
596   H···O hydrogen bond lengths in minerals. Monatshefte Für Chemie,
597   130, 1047–1059.
598   Lower, S.K., Maurice, P.A., and Traina, S.J. (1998) Simultaneous
599   dissolution of hydroxylapatite and precipitation of
600   hydroxypyromorphite: direct evidence of homogeneous nucleation.
601   Geochimica et Cosmochimica Acta, 62, 1773–1780.
602   Ma, Q.Y., Logan, T.J., and Traina, S.J. (1995) Lead Immobilization from
603   Aqueous Solutions and Contaminated Soils Using Phosphate Rocks.
604   Environmental Science & Technology, 29, 1118–1126.
605   Mavropoulos, E., Rossi, A.M., Costa, A.M., Perez, C.A.C., Moreira, J.C.,
606   and Saldanha, M. (2002) Studies on the Mechanisms of Lead
607   Immobilization by Hydroxyapatite. Environmental Science &
608   Technology, 36, 1625–1629.
609   Nguyen, C.K., Stone, K.R., and Edwards, M.A. (2011) Chloride-to-sulfate
610   mass ratio: Practical studies in galvanic corrosion of lead solder.
611   Journal - American Water Works Association, 103, 81–92.
612   Pasero, M., Kampf, A.R., Ferraris, C., Pekov, I.V., Rakovan, J., and White,
613   T.J. (2010) Nomenclature of the apatite supergroup minerals.
614   European Journal of Mineralogy, 22, 163–179.
615   Peters, N.J., Davidson, C.M., Britton, A., and Robertson, S.J. (1999) The
616   nature of corrosion products in lead pipes used to supply drinking
617   water to the City of Glasgow, Scotland, UK. Fresenius' Journal of
618   Analytical Chemistry, 363, 562–565.
619   Shannon, R.D., and Prewitt, C.T. (1969) Effective ionic radii in oxides and
620   fluorides. Acta Crystallographica, B25, 925–946.
621   Sheldrick, G.M. (2015a) SHELXT - Integrated space-group and crystal-
622   structure determination. Acta Crystallographica, A71, 3–8.
623   Sheldrick, G.M. (2015b) Crystal structure refinement with SHELXL. Acta
624   Crystallographica, C71, 3–8.
625   Stock, M.J., Humphreys, M.C.S., Smith, V.C., Johnson, R.D., Pyle, D.M.,
626   and EIMF (2015) New constraints on electron-beam induced halogen
627   migration in apatite. American Mineralogist, 100, 281–293.
628   Stormer, J.C., Pierson, M.L., and Tacker, R.C. (1993) Variation of F and Cl
629   X-ray intensity due to anisotropic diffusion in apatite during electron
630   microprobe analysis. American Mineralogist, 78, 641–648.
631   Sudarsanan, K., and Young, R.A. (1978) Structural interactions of F, Cl and
632   OH in apatites. Acta Crystallographica Section B, 34, 1401-1407.
633   Temple, A.K. (1956) V.—The Leadhills-Wanlockhead Lead and Zinc
634   Deposits. Transactions of the Royal Society of Edinburgh, 63, 85–
635   113.
636   US Environmental Protection Agency (USEPA) (2019) Optimized Corrosion
637   Control Treatment Evaluation Technical Recommendations for
638   Primacy Agencies and Public Water Systems (Online). Available:
639   https://www.epa.gov/sites/production/files/2019-

640   07/documents/occtmarch2016updated.pdf (accessed July 18, 2020)
641   USEPA, Washington.
642   Valsami-Jones, E., Ragnarsdottir, K.V., Putnis, A., Bosbach, D., Kemp, A.J.,
643   and Cressey, G. (1998) The dissolution of apatite in the presence of
644   aqueous metal cations at pH 2–7. Chemical Geology, 151, 215–233.
645   White, T.J., and ZhiLi, D. (2003) Structural derivation and crystal chemistry
646   of apatites. Acta Crystallographica, B59, 1–16.
647   Zhu, Y., Huang, B., Zhu, Z., Liu, H., Huang, Y., Zhao, X., and Liang, M.
648   (2016) Characterization, dissolution and solubility of the
649   hydroxypyromorphite–hydroxyapatite solid solution
650          $[(Pb_xCa_{1-x})_5(PO_4)_3OH]$ at 25 °C and pH 2–9. Geochemical
651   Transactions, 17, 1–18.

652
653
654

FIGURE CAPTIONS

657   Figure 1. Aggregates of prismatic hydroxylpyromorphite crystals on quartz.
658   Horizontal field of view is 0.45 mm.

660   Figure 2. SEM image of hydroxylpyromorphite crystals.

662   Figure 3. The infrared spectrum of hydroxylpyromorphite from 4000 to 650
663   cm^{-1}.

665   Figure 4. The structure of hydroxylpyromorphite as viewed down the *c* axis.
666   Lead (shades of gray), phosphorus (green), oxygen of hydroxyl molecules
667   (red).

669   Figure 5. Hypothetical local configurations of the anion column for (A) end-
670   member hydroxylpyromorphite and (B) hydroxylpyromorphite containing
671   fluoride.

673   Figure 6. A comparison of column anion arrangements in pyromorphite and
674   other apatite group minerals. Hydroxylpyromorphite (this work),
675   pyromorphite (Dai and Hughes, 1989), $Pb_5(PO_4)_3F$ (Fleet et al., 2010),
676   hydroxylapatite (Hughes et al., 1989), chlorapatite (Kelly et al., 2017). Lead
677   (dark gray), fluorine (green), oxygen (red), calcium (light blue), chlorine
678   (magenta), hydrogen (light gray).

680   Figure S1. Change in $FK\alpha$ X-ray counts over time in the electron
681   microprobe of hydroxylpyromorphite type material; suggesting no
682   significant electron beam induced migration of F.

683
684
685
686
687
688
689

24

690   Table 1. Chemical composition (in wt%) for hydroxylpyromorphite.

Constituent	Mean	Range	Stand. Dev.	Standard
PbO	82.20	80.21-83.63	1.19	galena
P_2O_5	15.77	14.54-16.33	0.67	fluorapatite
Cl	0.15	0.10-0.28	0.05	tugtupite
F	0.46	0.23-0.69	0.21	LiF
H_2O*	0.46			
O=Cl	-0.03			
O=F	-0.19			
Total	98.82			

691   * based on the structure

692

693   Table 2. Comparison of powder diffraction data, I and d (Å), for
694   hydroxylpyromorphite of different origins. fs = fairly strong, vs = very
695   strong, vw = very weak, b = broad, bb = very broad

Whytes Cleuch (Temple 1956)		Rabenwald*		Synthetic (Hey 1950)		Copps mine (This work)	
fs	4.06	fs	4.05	24	4.03	18	4.08
vw	3.56	w	3.56	16	3.61	6	3.67
vw	3.18	wb	3.23	16	3.18	21	3.21
vs	2.92	vs	2.90	100	2.91	100	2.93
vw	2.82	vwb	2.37	8	2.82	13	2.82
w	2.02	vw	2.02	16	2.02	21	2.04
vw	1.96	vw	1.97	8	1.96	9	1.98
w	1.91	vw	1.93	16	1.91	23	1.94
vw	1.88	w	1.88	8	1.86	15	1.85
vw	1.82	wb	1.83	16	1.82	24	1.83
vw	1.56	vwbb	1.59	8	1.57	17	1.59
vw	1.51	vwbb	1.50	16	1.51	10	1.49

696   *Uwe Kolitsch personal communication, May 2018. Data obtained using a KappaCCD
697   single-crystal diffractometer, Gandolfi-like digital powder pattern, MoKα, crystal-detector
698   distance 38 mm.

699

700

701   Table 3. Comparison of crystallographic data for hydroxylpyromorphite to
702   various synthetic pyromorphites.

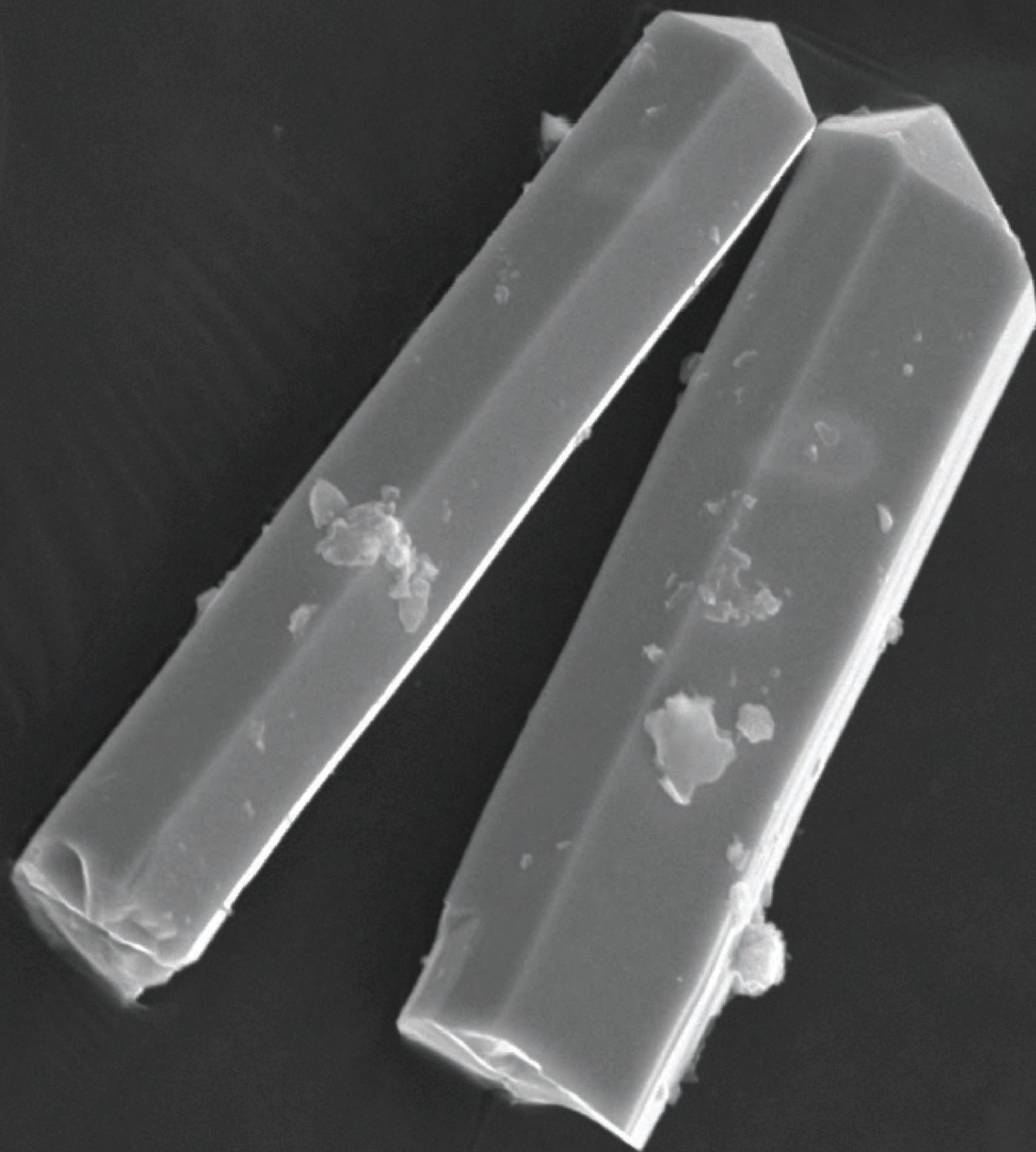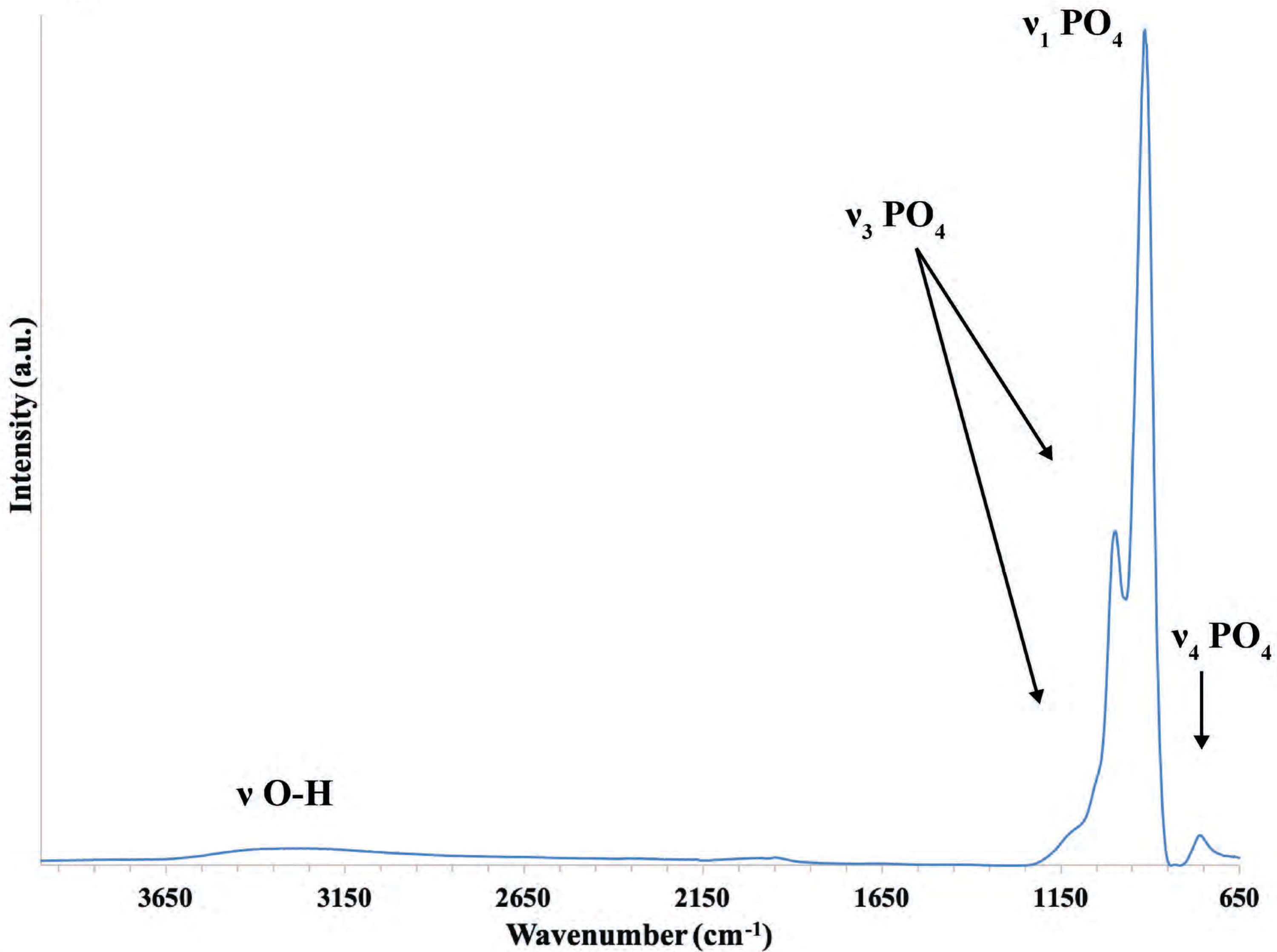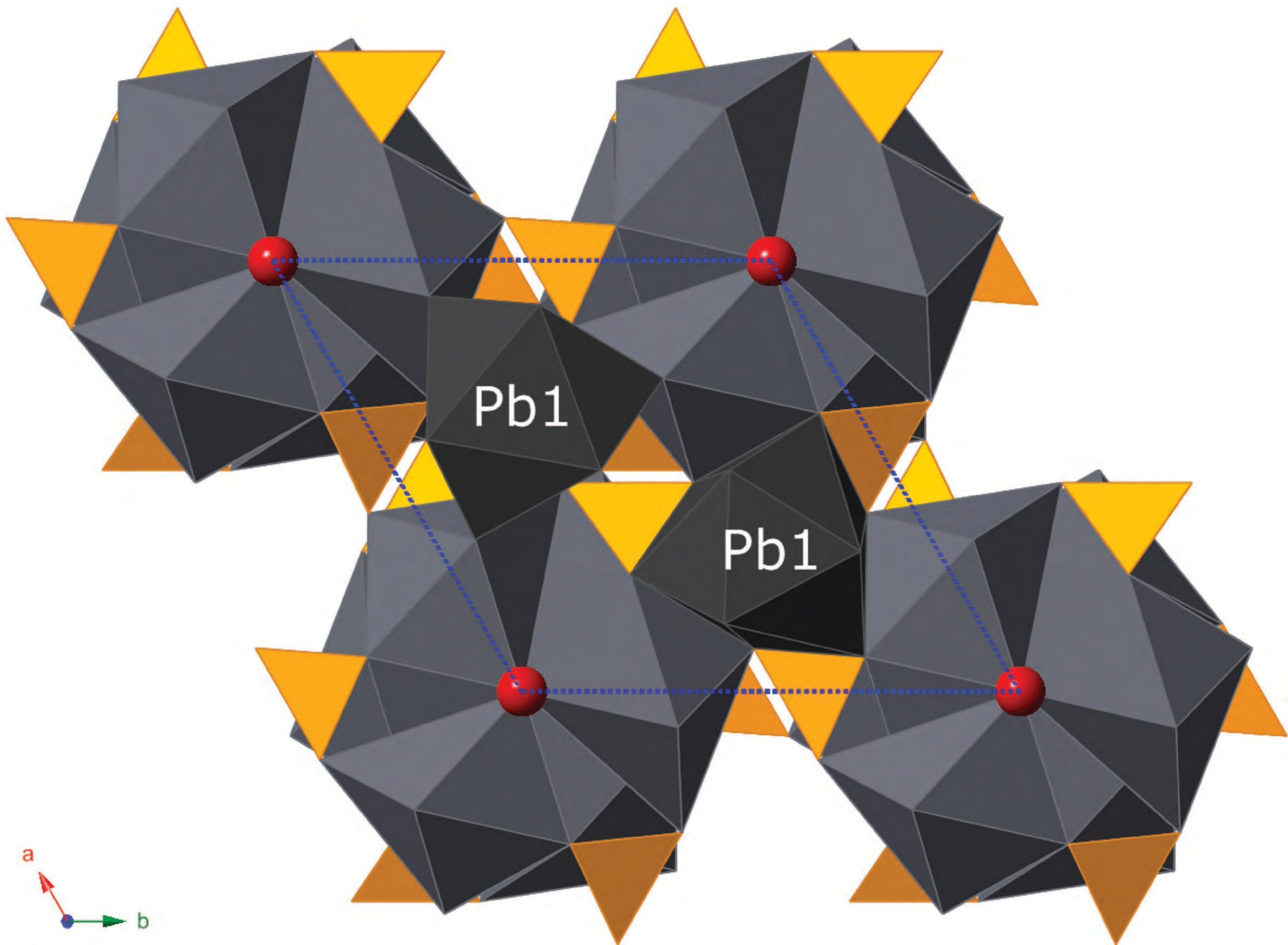|	hydroxylpyromorphite (This work)	$Pb_5(PO_4)_3OH$ (Barinova *et al.*, 1998)	$Pb_5(PO_4)_3OH$ (Brückner *et al.*, 1995)	$Pb_5(PO_4)_3F$ (Fleet *et al.*, 2010)	$Pb_5(PO_4)_3F$ (Belokoneva *et al.*, 1982)
a (Å)	9.7872(14)	9.774(1)	9.866(3)	9.7638(6)	9.760(8)
c (Å)	7.3070(10)	7.291(1)	7.426(2)	7.2866(4)	7.300(8)
V (Å^3)	606.2	603.2	625.9	601.6	602.2
Calculated density	7.340	7.356	7.177	7.397	7.389
<Pb1–O>	2.703	2.701	2.767	2.696	2.714
<Pb2–O/F>	2.708	2.702	2.703	2.704	2.683
<Pb2—Pb2>	4.314	3.961	4.227	3.953	4.327
Pb2–OH/F	2.932/2.58	2.925	2.896	2.752	2.954
<P1–O>	1.544	1.539	1.509	1.533	1.566
Pb1 metaprism twist angle (°)	21.6	22.1	26.7	22.7	23.6

703
704
705
706
707
708

Figure 1
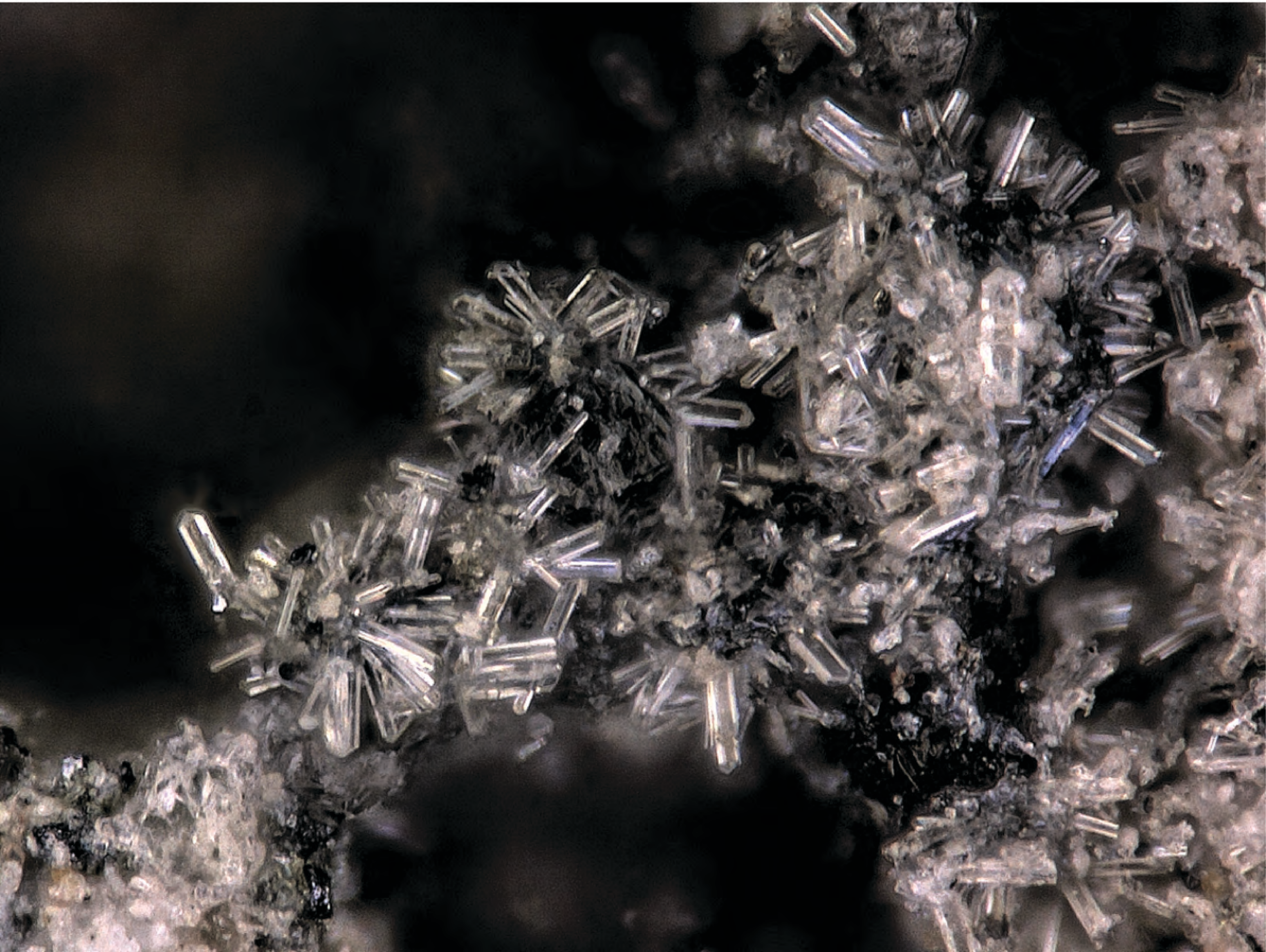
Figure 2

10 µm

Figure 3

Figure 4

Figure 5

Figure 6

hydroxylpyromorphite pyromorphite Pb$_5$(PO$_4$)$_3$F hydroxylapatite chlorapatite

$z=1/4$

$z=0$

$z=1/4$

c c c c c